Electrochemistry

International Edition: DOI: 10.1002/anie.201505290
German Edition: DOI: 10.1002/ange.201505290

# Rerouting Electron Transfer in Molecular Assemblies by Redox-Pair Matching

*Renata Balgley, Sreejith Shankar, Michal Lahav,* and Milko E. van der Boom**

***Abstract:*** *We demonstrate how the distance over which electron transfer occurs through organic materials can be controlled and extended. Coating of conductive surfaces with nanoscale layers of redox-active metal complexes allows the electrochemical addressing of distant layers that are otherwise electrochemically silent. Our materials can pass electrons selectively in directions that are determined by positioning of layers of metal complexes and the distances between them. These electron-transfer processes can be made dominantly uni- or bidirectional. The design involves 1) a set of isostructural metal complexes with different electron affinities, 2) a scalable metal–organic spacer, and 3) a versatile assembly approach that allows systematic variation of composition, structure, and electron-transfer properties. We control the electrochemical communication between interfaces by the deposition sequence and the spacer length, therefore we are able to program the bulk properties of the assemblies.*

The development of molecular materials to be used as functional elements in semiconductor-based devices has witnessed an increasing interest in the recent years. The design of such materials is stimulated by forecasts that silicon technology is reaching its scalability limits.[1–3] Chemical modification of inorganic surfaces, aimed at designing functional materials with specifically tailored properties, requires deposition processes with molecular-level control.[4–9] Although much progress has been made in understanding electron transfer (ET) in organic materials, the design of functional materials with well-defined ET properties is still a tremendous challenge.[10,11] Restriction of ET to one direction has been observed with redox polymers and electrodeposited films.[12–15] Electrochemical rectification using redox mediators, in solution or surface-adhered, has been recognized and demonstrated by Murray, Bard, and Wrighton, and their respective co-workers.[12,13,16–19] In addition, rectification with monolayer-based transistors has been reported recently.[20,21] Nevertheless, no general approach is available for the fabrication of one kind of surface-confined organic materials that exhibit a variety of ET properties. Ideally, a versatile assembly strategy using a single set of components would generate a series of materials that exhibit scalable interlayer communication that is uni- or bidirectional. Such fundamentally important ET characteristics might result in practical molecular devices (e.g., sensors,[22] memory,[23] and electronic elements[24–26]).

Herein, we introduce composite materials that exhibit molecularly designed and scalable interlayer ET properties. Functionalization of common metal-oxide electrodes with redox-active and robust ruthenium (**1**) and osmium (**2**) complexes results in electrochemical addressing of additional but distant iron (**3**) complexes that are otherwise electrochemically inactive. Our assembly strategy uses this set of different functional molecular components (**1**–**3**), and an organic molecule (BPEB) to generate a scalable metal–organic spacer (Figure 1). These components exhibit similar coordination chemistry towards palladium(II). Palladium dichloride links all these components by binding through terminal pyridine groups. Coating of metal-oxide electrodes using different solution-deposition sequences of the compounds (**1**–**3** and BPEB) allows control of the electronic communication between interfaces consisting of the metal complexes (**1**–**3**). The directionality of the ET processes is controlled by the materials composition, whereas the ET efficiency is defined by the length of the spacer $BPEB_n$.

In a previous report,[27] we have shown that a simple two-component system consisting of layers of ruthenium and osmium polypyridyl complexes exhibits unidirectional electrochemical behavior based on the sequence of deposition. This system undergoes catalytic redox reactions in one of two possible directions. In the present study, we use potential matching between different layers and introduce a scalable organic spacer. These layers consist of polypyridyl complexes of the Fe/Ru/Os triad or a combination thereof. The spacer allows precise control over the thickness, separation, and positioning of the electroactive layers, the ET pathway, and the electrochemical communication between the layers of metal complexes. A judicious combination of the independent components results in different modular assemblies that exhibit diverse and controllable ET properties. These unique functionalities are not achievable with our two-component system without the scalable organic spacer. The additional level of complexity of our new systems presented here demonstrates the high degree of control over their properties.

In this study we report on four molecular assemblies (**MA1**–**4**) with different materials configurations that are formed by using the same procedure (Figure 1). **MA1** ($BPEB_n$-Fe) consists of a nanoscale layer of complex **3** on top of a $BPEB_n$ spacer, with the spacer connected via an organic layer (TPEB), which is electrochemically inactive in the studied potential range, to the ITO electrode (Scheme

[*] R. Balgley, Dr. S. Shankar, Dr. M. Lahav, Prof. M. E. van der Boom
Department of Organic Chemistry
The Weizmann Institute of Science
7610001 Rehovot (Israel)
E-mail: michal.lahav@weizmann.ac.il
milko.vanderboom@weizmann.ac.il

Supporting information for this article is available on the WWW under http://dx.doi.org/10.1002/anie.201505290.

  

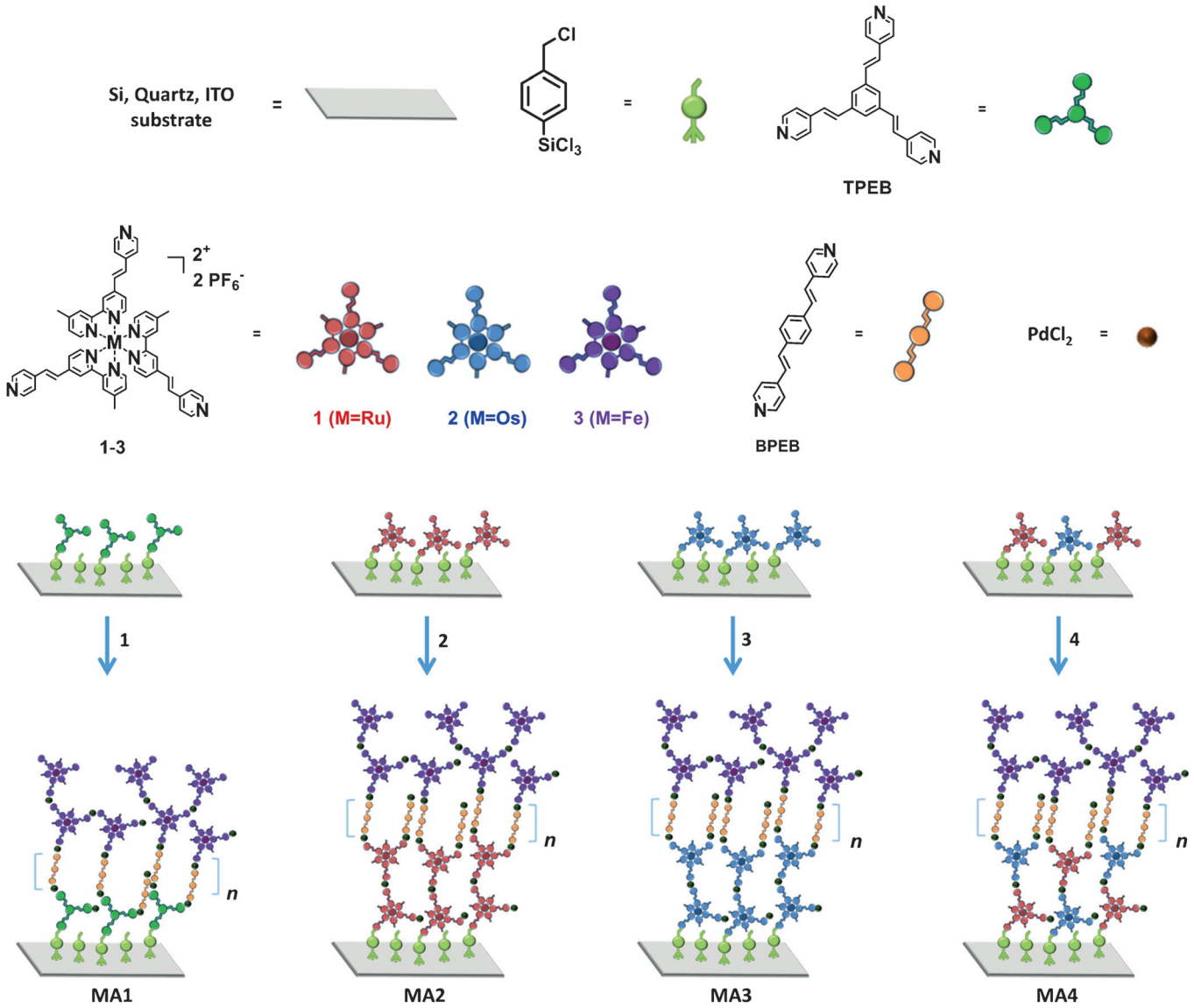


***Figure 1.*** Formation and composition of coordination-based molecular assemblies (MAs). The MAs are formed on a surface-bound layer based on TPEB, **1**, **2**, or on a mixture of complexes **1** and **2. MA1**, sequence 1: *n* depositions of BPEB ($n = 0$–10) and two depositions of **3. MA2**–**4**, sequences 2–4: one deposition of **1** (**MA2**), **2** (**MA3**), or a mixture of complexes **1** and **2** (**MA4**), *n* depositions of BPEB ($n = 0$–15), and two depositions of **3**. There is a deposition step of $PdCl_2$ between each deposition of the molecular components.

S1A in the Supporting Information). The other three assemblies, namely **MA2** (Ru-$BPEB_n$-Fe), **MA3** (Os-$BPEB_n$-Fe), and **MA4** ((Ru-Os)-$BPEB_n$-Fe) also consist of a layer of complex **3** on top of a $BPEB_n$ spacer. The spacer, in these three MAs, is connected via a redox-active layer of **1** (Ru) or **2** (Os), or both complexes (**1**–**2**) to the ITO electrode (Scheme S1B). This bottom-up approach resulted in two interesting materials features: 1) Interlayer ET: For all assemblies, the use of relatively short $BPEB_n$ spacers results in reversible electrochemical behavior of the metal complexes (**1**–**3**). For **MA1**, increasing the $BPEB_n$ length suppressed the communication between the iron complexes (**3**) and the electrode. For **MA2**–**4**, we connected complexes **1** and/or **2** directly to the electrode surface. The presence of these redox-active ruthenium (**1**) and osmium (**2**) complexes resulted in electrochemical addressing of the iron complexes (**3**) that are otherwise silent. Thus, the distance over which ET occurs through the assembly can be controlled and extended. 2) Rerouting ET: The differences in the redox potentials of the components (**1**–**3**) of these four assemblies (**MA1**–**4**) result in substantially different electrochemical characteristics. The nature of the redox-mediating metal centers (Os or Ru) determines the directionality of the current flow during a voltammetric cycle. For **MA2**, only unidirectional oxidative-catalytic current is observed, whereas for **MA3** a reductive-catalytic current is dominant, at a certain distance from the electrode. When both complexes **1** and **2** are used in one material (**MA4**), the distances by which the ET processes between the iron complexes (**3**) and the ITO electrode occur are not only enhanced, but also mediated in both oxidative and reductive directions. This effect confirms the mechanism operating with **MA2** and **MA3**, and it shows that it is possible

to include two opposing electron-transfer mediators in one layer.

All MAs were obtained by using an iterative solution-deposition process according to the assembly sequence presented in Figure 1. Immersion of monolayer-functionalized substrates (see the Supporting Information for details) in solutions of common organic solvents containing a palladium salt ($[Pd(PhCN)_2Cl_2]$) were followed by immersion in solutions of the redox-active metal complexes (**1** and/or **2**, or **3**), or BPEB. The palladium salt serves as a cross-linker between the different pyridine-terminated interfaces. The number of depositions of BPEB to generate the interlayer spacer was systematically varied from 0 to 15. The films were characterized by optical spectroscopy (UV/Vis and ellipsometry), X-ray photoelectron spectroscopy (XPS), and atomic force microscopy (AFM) to determine their composition, growth, thickness, and structure, whereas electrochemistry (cyclic voltammetry) was used to demonstrate their rich, diverse, and controllable ET properties. The UV/Vis absorption of complexes **1**–**3** is similar.[28,29] Therefore, all MAs exhibit a strong absorption band at approximately $\lambda = 320$ nm (Figure 2), which is characteristic of a ligand-centered π–π* transition.

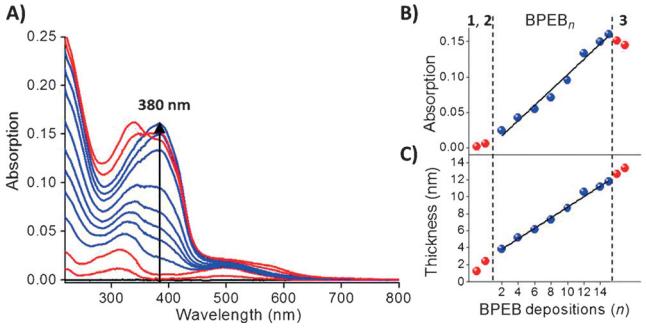


***Figure 2.*** UV/Vis spectroscopy and spectroscopic ellipsometry analysis of (Ru-Os)-BPEB$_n$-Fe (**MA4**). A) Optical absorption measured on quartz. The bottom red traces represent the absorption spectra of ruthenium (**1**) and osmium (**2**) complexes. The top red traces represent the absorption spectra of **MA4** including the iron complex (**3**) layers. The blue traces represent the absorption spectra of (Ru-Os)-BPEB$_n$ (even deposition cycles of BPEB/$PdCl_2$). B) Absorption intensity at $\lambda = 380$ nm vs. the number of deposition cycles (linear fit; $R^2 = 0.98$). C) Ellipsometry-derived thickness versus the number of deposition cycles measured on silicon (linear fit; $R^2 = 0.99$). The bottom and the top red symbols represent the absorption (B) and thickness (C) of the MAs including the metal complexes (**1**, **2**, and **3**).

Their metal-to-ligand charge transfer ($^1$MLCT) bands are observed between $\lambda = 490$–$555$ nm. The absorption band of the BPEB$_n$ spacer is centered at $\lambda = 380$ nm and its intensity increases linearly with the number of BPEB/$PdCl_2$ deposition cycles (Figure 2B, and Figures S3B, S4B, and S5B). Likewise, linear growth was indicated by spectroscopic ellipsometry (Figure 2C and Figures S3C, S4C, and S5C). A linear correlation between the BPEB absorption band maximum and the BPEB thickness (Figure S6) demonstrates the homogeneity of our assemblies and corroborates the constant amount of BPEB being deposited in each deposition cycle. Our deposition strategy allows sub-nanometer separation of the redox-active layers up to 9.5 nm with regular intervals of 0.5 nm.

To determine the maximum electrochemically addressable distance between the ITO electrode and the terminal layer consisting of iron complex **3**, we performed a series of CV experiments with **MA1**. The length of the spacer BPEB$_n$ was systematically varied from 1.0 nm ($n = 2$) to 5.5 nm ($n = 10$). The CVs of BPEB$_n$-Fe ($n = 2$, 8, 10) are shown in the insets of Figure 3A, B, and C, respectively, and in Figure S7. As expected, increasing the spacer length gradually reduces the $Fe^{2+/3+}$ redox wave currents until they completely disappear ($n = 10$). To enhance the distance over which the ET occurs and to control its directionality, we substituted the densely packed organic layer (TPEB)[30] with layers of the ruthenium (**1**) or osmium (**2**) complexes, and with an approximately 1:1 mixture of both complexes (**1**–**2**; Figure 1 and Scheme S1). The composition and the surface morphology were determined by electrochemistry, XPS, and AFM measurements (see the Supporting Information for details). These modifications of the ITO surface allow for higher currents to pass through our assemblies, resulting in electrochemical addressing of complexes **3** at much larger distances from the ITO electrode (up to 9.5 nm for **MA4** versus 5.5 nm for **MA1**).

**MA1** exhibits bidirectional ET behavior, however, the assemblies **MA2** and **MA3** can also display preferentially unidirectional but opposite ET. This rectifying behavior is a result of the different electron affinity of the Ru/Fe (**MA2**), and Os/Fe (**MA3**) couples. The cyclic voltammograms (CVs) of Ru-BPEB$_n$-Fe and Os-BPEB$_n$-Fe exhibit catalytic waves associated with the $Fe^{2+/3+}$ redox couple (Figure 4) at distances from the surface (5.5–9.5 nm) where the electrochemical activity of complex **3** is suppressed in BPEB$_n$-Fe (Figure 3B, inset).

For Ru-BPEB$_n$-Fe (**MA2**), the oxidative-catalytic ET from the iron complexes (**3**) towards the electrode can be observed in the corresponding CV (Figure 4, purple curve). This electrochemical measurement starts at a low potential (0.4 V) with both ruthenium (**1**) and iron (**3**) complexes in their reduced state ($Ru^{2+}$ and $Fe^{2+}$). The insulating BPEB$_n$ spacer (4.0–6.0 nm, $n = 7$–$10$), prohibits the oxidation of complex **3** at the expected half-wave potential ($E_{1/2} = 0.97$ V). Small amounts of $Ru^{3+}$ are generated at the onset potential of the oxidation of the ruthenium complexes (**1**) at 1.0 V. The thermodynamic parameters permit the oxidation of $Fe^{2+}$ to $Fe^{3+}$ by $Ru^{3+}$. The $Ru^{3+}$ centers are constantly regenerated by the ITO electrode at this potential, therefore, a catalytic channel for the oxidation of the upper iron complexes (**3**) is generated (Figure 4, pathway 1).[12,13] This ruthenium-mediated ET is primarily unidirectional, resulting in a sharp oxidative-catalytic wave. The nature of the $Fe^{2+/3+}$ oxidation wave depends on the BPEB$_n$ thickness (Figure S8, purple curves, and Table S1). Increasing the spacer length above 4.0 nm, the $Fe^{2+/3+}$ anodic wave transforms from a reversible to a catalytic one. This transformation can be characterized by: 1) the overpotential required to oxidize the iron complex **3**, which is expressed by an increase in the anodic peak potential ($E_{ap}$), and 2) the decrease in the half width at half maximum (HWHM) of the oxidation wave

  

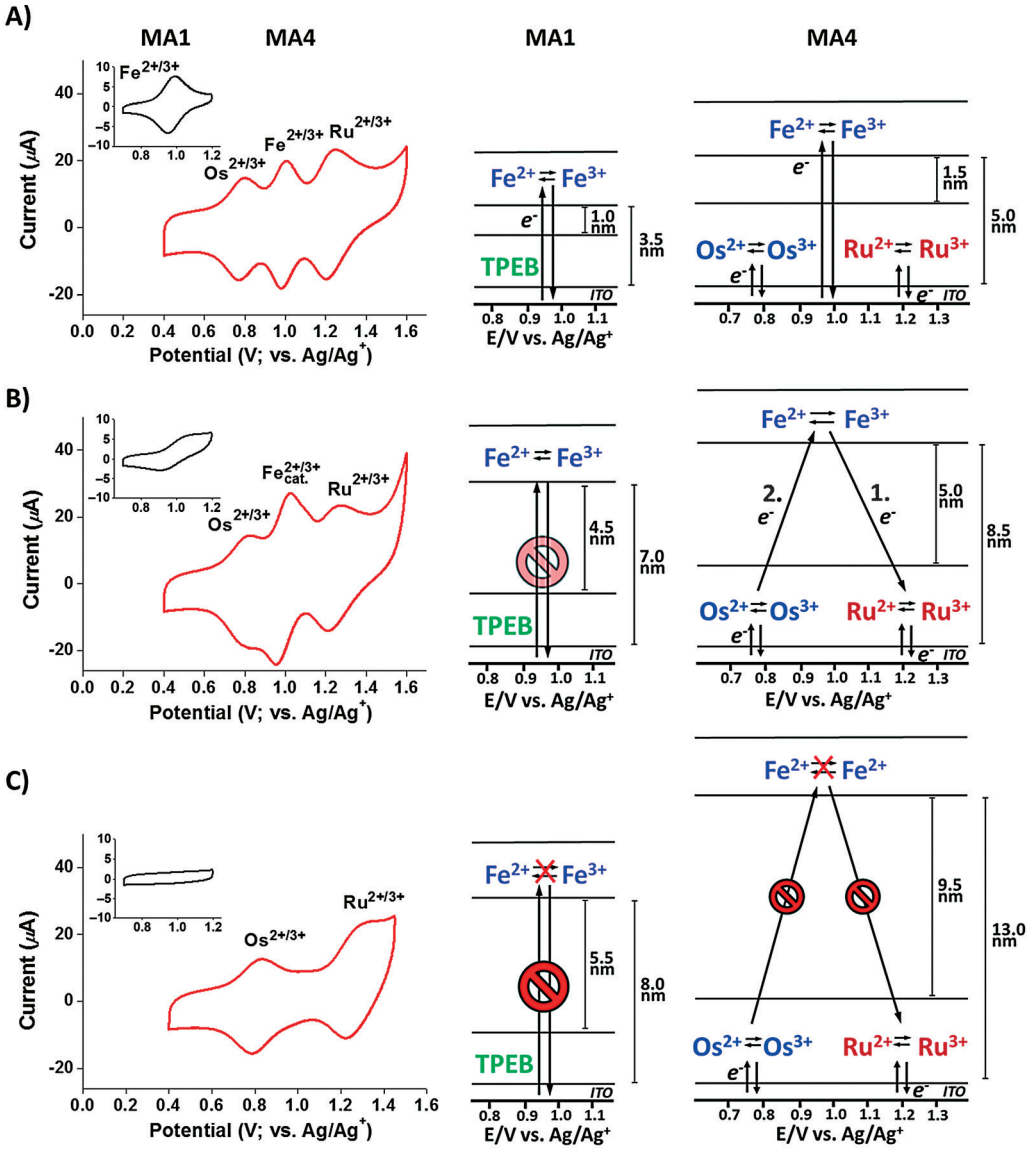


*Figure 3.* Representative cyclic voltammograms of BPEB$_n$-Fe (**MA1**) and (Ru-Os)-BPEB$_n$-Fe (**MA4**) and the corresponding electron transfer (ET) schemes. The CVs of **MA1** (insets) and **MA4** are shown in the left column with increasing BPEB$_n$ spacing (A–C). The BPEB$_n$ thickness and the number of BPEB depositions ($n$) are: A) 1.5 nm $n=2$, inset: 1.0 nm, $n=2$; B) 5.0 nm, $n=8$; inset: 4.5 nm, $n=8$; C) 9.5 nm, $n=15$; inset: 5.5 nm, $n=10$. Inset axes: Current (μA) vs. potential (V; vs. Ag/Ag$^+$). The corresponding ET schemes **MA1** (center column) and **MA4** (right column): A) Direct ET between the ITO and the Fe centers (**3**) occurs in both **MA1** and **MA4**. B) ET between the ITO and **3** is suppressed for **MA1**. For **MA4**, catalytic ET occurs: pathway 1 corresponds to the oxidative-catalytic direction and pathway 2 corresponds to the reductive-catalytic direction. C) The Fe centers (**3**) are electrochemically isolated in both **MA1** and **MA4**. The CVs were recorded at 100 mV s$^{-1}$ using ITO, Pt wire, and Ag wire as the working, counter, and reference electrodes, respectively.

(from 60 mV when the BPEB$_n$ thickness is less than 4.0 nm to 40 mV when the thickness is greater than 4.0 nm). Lower HWHM values result in the appearance of a sharp catalytic peak, as expected from its generation at the onset potential of the redox mediator **1**. Reversing the potential results in the reduction of $Ru^{3+}$ to $Ru^{2+}$ ($E_{1/2}=1.22$ V), however, the $Fe^{3+}$ centers remain trapped in their oxidized state because no reductive pathway is accessible. The diminished heights of the $Fe^{2+/3+}$ oxidative-catalytic wave in the consecutive CV scans are due to charge trapping (Figure S9). This charge can be released by applying a negative potential bias in the reverse scan direction, which regenerates the initial catalytic wave.

For Os-BPEB$_n$-Fe (**MA3**), reductive-catalytic ET occurs (Figure 4, green curve). This catalytic reduction of $Fe^{3+}$ centers is mediated by traces of $Os^{2+}$ formed at the onset potential of $Os^{3+}$ reduction (ca. 1.0 V) and is favored over the nonmediated reduction (Figure 4, pathway 2). Hence, a catalytic wave of negative current is formed at $E_{1/2}=0.91$ V. A similar trend in the cathodic peak potential ($E_{cp}$) and in the HWHM of the iron complex **3** is seen for **MA3** (70 mV for BPEB$_n$ less than 4.0 nm thick and 60 mV for BPEB$_n$ more than 4.0 nm thick), compared to **MA2**, when increasing the spacer length (Figure S8, green curves, and Table S1).

The catalytic behavior of both Os-BPEB$_n$-Fe and Ru-BPEB$_n$-Fe results in an opposite ET directionality and its selectivity is scan-rate dependent (Figure S8 and Table S1).[28] Increasing the scan rate results in a more pronounced catalytic pathway, as evident by sharpening and potential shifts of the catalytic waves (increasing $E_{ap}$ value for **MA2** and decreasing $E_{cp}$ value for **MA3**), and suppressing of back ET pathways. For example, increasing the scan rate from 100 mV s$^{-1}$ to 500 mV s$^{-1}$ for Ru-BPEB$_7$-Fe (4.0 nm thick spacer) shifts the anodic peak to higher potentials (from $E_{ap}=1.04$ V to $E_{ap}=1.12$ V) and eliminates the cathodic wave (Figure S8 D–F, purple curves). Thus, the material composition controls the ET directionality, whereas the intensity and selectivity can be adjusted as a function of the rate of the potential sweeping.

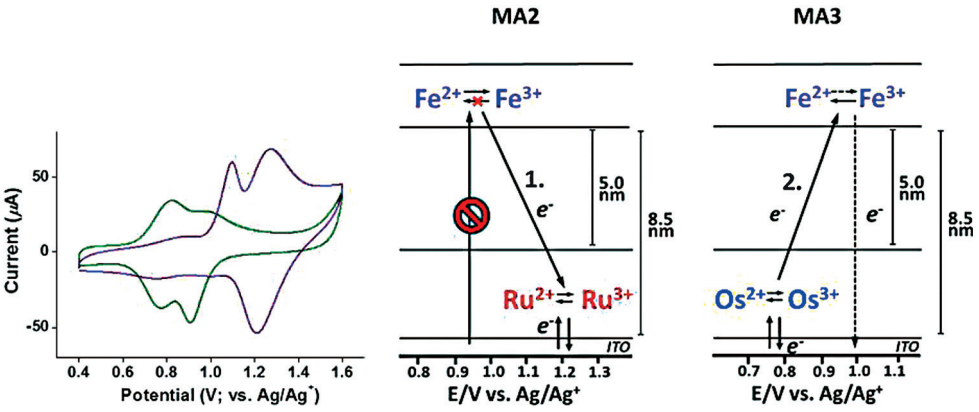


***Figure 4.*** Cyclic voltammograms of Ru-BPEB$_8$-Fe (**MA2**) and Os-BPEB$_9$-Fe (**MA3**) and the corresponding electron transfer schemes. The CVs of **MA2** (purple) and **MA3** (green) show the catalytic behavior for BPEB$_n$ = 5.0 nm. The corresponding scheme for **MA2** shows the ET in the oxidative direction (pathway 1) mediated by the Ru centers (**1**). For **MA3**, the ET is mediated in the reductive direction (pathway 2) by the Os centers (**2**). The CVs were recorded at 100 mV s$^{-1}$ using ITO, Pt wire, and Ag wire as the working, counter, and reference electrodes, respectively.

The structurally complex **MA4** (Ru-Os)-BPEB$_n$-Fe contains both ruthenium (**1**) and osmium (**2**) complexes at the bottom domain, which serves as a bidirectional catalytic gate for both the oxidation and the reduction of the upper domain (**3**). Also in this setup, the electrochemical accessibility of the iron complexes **3** is a function of the spacer length: 1) For BPEB$_n$ thicknesses less than 3.5 nm ($n$ = 0–6), complex **3** is directly accessible electrochemically by the electrode ($E_{1/2}$ = 0.97 V). The $Os^{2+/3}$ and $Ru^{2+/3+}$ redox couples are observed at $E_{1/2}$ = 0.7 and 1.22 V, respectively (Figure 3 A). 2) For BPEB$_n$ thicknesses ranging from 3.5 nm to 6.0 nm ($n$ = 7–10), complexes **3** are addressed in an oxidative and a reductive catalytic mode by traces of $Ru^{3+}$ (**1**) and $Os^{2+}$ (**2**), respectively (Figure 3 B). Gradually increasing the BPEB$_n$ thickness in this nanometer-scale range results in an overlap between the Fe catalytic waves with the Ru anodic and Os cathodic waves. The waves associated with Ru and Os increase symmetrically with concurrent disappearance of the waves associated with Fe (Figure S10). The ET characteristics of this MA are clearly a combination of the electrochemical properties of the individual components of Ru-BPEB$_n$-Fe and Os-BPEB$_n$-Fe. This contribution is seen by the increased peak currents of the $Fe^{2+/3+}$ redox couple, going from a reversible redox regime ($I_{ap}$ = 20 μA, $I_{cp}$ = 18 μA; Figure 3 A) to a catalytic regime ($I_{ap}$ = 27 μA, $I_{cp}$ = 24 μA; Figure 3 B), the same trend as for the individual **MA2** and **MA3** (Figure 4). BPEB and the ligands of complexes **1**–**3** are electrochemically inert at the studied potential range (0.4–1.6 V). These ligands undergo redox reactions at highly negative potentials (less than −0.6 V for **1**–**3** and less than −0.2 V for BPEB; Figure S11). 3) For BPEB$_n$ thicknesses greater than 6.0 nm ($n$ > 10), the upper domain (**3**) becomes electrochemically isolated as the Ru anodic wave and the Os cathodic wave regain their original peak currents ($I_{ap}$ = 23 μA, $I_{cp}$ = 16 μA; Figure 3 C).

In summary, we have introduced a versatile assembly strategy to control and direct the ET routes in a series of composite metal–organic materials. By using three isostructural complexes consisting of the iron–ruthenium–osmium triad, a scalable organic spacer and palladium pyridyl coordination chemistry, we designed materials with defined and restricted ET pathways. Unidirectional and opposite ET is achieved and controlled by generating well-separated and homogeneous layers of complexes with different redox potentials that thermodynamically allow either oxidation or reduction. In our setup, we demonstrate ET rerouting by varying the potential gradient between the layers consisting of the Os/Ru and Fe complexes; the rectification (only oxidation direction) was observed with the layers consisting only of the Ru complex (**MA2**). By combining the individual components of these materials into one film, bidirectional current flow through different pathways was demonstrated. Although bidirectional rectification might be possible with a single complex using our layered structure (M-BPEB$_n$-M with M = **1**, **2**, or **3**), these composite assemblies provide an in-depth understanding of the interfacial ET processes and a sufficient resolution of the voltammetric signals. Another important finding is the enhancement of the distances over which otherwise silent redox-active species can be addressed. This strategy offers important advantages compared to reported film fabrication methods, since one set of components and method can be used to tailor the full spectrum of electrochemical properties. A variety of such useful properties have been demonstrated here by placing the functional components in well-defined positions. The large range of possible combinations of different redox species and their spatial arrangements makes this a general approach to determine ET routes in thin films.[10,14,31–34]

## Acknowledgements

This research was supported by the Ministry of Science, Technology & Space, Israel, the Helen and Martin Kimmel Center for Molecular Design, Mary and Tom Beck-Canadian Center for Alternative Energy Research, David Rosenberg (Chicago, IL), the Yeda-Sela Center for Basic Research, a research grant from the Leona M. and Harry B. Helmsley Charitable Trust, and the Israel Science Foundation (ISF) Grant No. 289/09. We thank Dr. T. Bendikov (WIS) for carrying out the XPS experiments. M.E.vdB. is the incumbent of the Bruce A. Pearlman Professional Chair in Synthetic Organic Chemistry.

**Keywords:** electrochemistry · electron transfer · metal complexes · redox mediators · thin films

  

**How to cite:** *Angew. Chem. Int. Ed.* **2015**, *54*, 12457 – 12462
*Angew. Chem.* **2015**, *127*, 12634 – 12639

[1] C. Joachim, J. K. Gimzewski, A. Aviram, *Nature* **2000**, *408*, 541 – 548.
[2] J. C. Genereux, J. K. Barton, *Nat. Chem.* **2009**, *1*, 106 – 107.
[3] J. S. Lindsey, D. F. Bocian, *Acc. Chem. Res.* **2011**, *44*, 638 – 650.
[4] R. P. Ortiz, A. Facchetti, T. J. Marks, *Chem. Rev.* **2010**, *110*, 205 – 239.
[5] C. Simão, M. Mas-Torrent, N. Crivillers, V. Lloveras, J. M. Artés, P. Gorostiza, J. Veciana, C. Rovira, *Nat. Chem.* **2011**, *3*, 359 – 364.
[6] Y. Xia, G. M. Whitesides, *Angew. Chem. Int. Ed.* **1998**, *37*, 550 – 575; *Angew. Chem.* **1998**, *110*, 568 – 594.
[7] R. D. Piner, J. Zhu, F. Xu, S. Hong, C. A. Mirkin, *Science* **1999**, *283*, 661 – 663.
[8] L. Scheres, J. ter Maat, M. Giesbers, H. Zuilhof, *Small* **2010**, *6*, 642 – 650.
[9] A. Ulman, *Chem. Rev.* **1996**, *96*, 1533 – 1554.
[10] R. Sakamoto, S. Katagiri, H. Maeda, H. Nishihara, *Coord. Chem. Rev.* **2013**, *257*, 1493 – 1506.
[11] N. Tuccitto, V. Ferri, M. Cavazzini, S. Quici, G. Zhavnerko, A. Licciardello, M. A. Rampi, *Nat. Mater.* **2009**, *8*, 41 – 46.
[12] H. D. Abruna, P. Denisevich, M. Umana, T. J. Meyer, R. W. Murray, *J. Am. Chem. Soc.* **1981**, *103*, 1 – 5.
[13] P. Denisevich, K. W. Willman, R. W. Murray, *J. Am. Chem. Soc.* **1981**, *103*, 4727 – 4737.
[14] D. M. DeLongchamp, M. Kastantin, P. T. Hammond, *Chem. Mater.* **2003**, *15*, 1575 – 1586.
[15] R. Kaminker, X. De Hatten, M. Lahav, F. Lupo, A. Gulino, G. Evmenenko, P. Dutta, C. Browne, J. Nitschke, M. E. van der Boom, *J. Am. Chem. Soc.* **2013**, *135*, 17052 – 17059.
[16] *Molecular Design of Electrode Surfaces* (Ed. R. W. Murray), Wiley, New York, **1992**.
[17] M. Arca, M. V. Mirkin, A. J. Bard, *J. Phys. Chem.* **1995**, *99*, 5040 – 5050.
[18] D. K. Smith, G. A. Lane, M. S. Wrighton, *J. Phys. Chem.* **1988**, *92*, 2616 – 2628.
[19] G. T. R. Palmore, D. K. Smith, M. S. Wrighton, *J. Phys. Chem. B* **1997**, *101*, 2437 – 2450.
[20] Y. Liu, B. Wolfrum, M. Hüske, A. Offenhäusser, E. Wang, D. Mayer, *Angew. Chem. Int. Ed.* **2013**, *52*, 4029 – 4032; *Angew. Chem.* **2013**, *125*, 4121 – 4124.
[21] C. A. Nijhuis, W. F. Reus, A. C. Siegel, G. M. Whitesides, *J. Am. Chem. Soc.* **2011**, *133*, 15397 – 15411.
[22] G. de Ruiter, T. Gupta, M. E. van der Boom, *J. Am. Chem. Soc.* **2008**, *130*, 2744 – 2745.
[23] R. Baron, A. Onopriyenko, E. Katz, O. Lioubashevski, I. Willner, S. Wang, H. Tian, *Chem. Commun.* **2006**, 2147 – 2149.
[24] R. L. Carroll, C. B. Gorman, *Angew. Chem. Int. Ed.* **2002**, *41*, 4378 – 4400; *Angew. Chem.* **2002**, *114*, 4556 – 4579.
[25] S. J. van der Molen, M. Calame, M. Reed, R. Naaman, E. Scheer, J. B. Neaton, A. Nitzan, D. Natelson, N. J. Tao, H. van der Zant, M. Mayor, M. Ruben, C. Grupe, *Nat. Nanotechnol.* **2013**, *8*, 385 – 389.
[26] N. Nerngchamnong, L. Yuan, D. C. Qi, J. Li, D. Thompson, C. A. Nijhuis, *Nat. Nanotechnol.* **2013**, *8*, 113 – 118.
[27] G. de Ruiter, M. Lahav, G. Evmenenko, P. Dutta, D. A. Cristaldi, A. Gulino, M. E. van der Boom, *J. Am. Chem. Soc.* **2013**, *135*, 16533 – 16544.
[28] S. Campagna, F. Puntoriero, F. Nastasi, G. Bergamini, V. Balzani, *Top. Curr. Chem.* **2007**, *280*, 117 – 214.
[29] D. Kumaresan, K. Shankar, S. Vaidya, R. H. Schmehl, *Top. Curr. Chem.* **2007**, *281*, 101 – 142.
[30] R. Kaminker, L. Motiei, A. Gulino, I. Fragalà, L. J. W. Shimon, G. Evmenenko, P. Dutta, M. A. Iron, M. E. van der Boom, *J. Am. Chem. Soc.* **2010**, *132*, 14554 – 14561.
[31] G. de Ruiter, M. Lahav, M. E. van der Boom, *Acc. Chem. Res.* **2014**, *47*, 3407 – 3416.
[32] D. M. Guldi, H. Nishihara, L. Venkataraman, *Chem. Soc. Rev.* **2015**, *44*, 842 – 844.
[33] S. Richter, C. H. H. Traulsen, T. Heinrich, J. Poppenberg, C. Leppich, M. Holzweber, W. E. S. Unger, C. A. Schalley, *J. Phys. Chem. C* **2013**, *117*, 18980 – 18985.
[34] P. C. Mondal, J. Yekkoni Lakshmanan, H. Hamoudi, M. Zharnikov, T. Gupta, *J. Phys. Chem. C* **2011**, *115*, 16398 – 16404.

Received: June 9, 2015
Revised: August 6, 2015
Published online: September 10, 2015

  